

1           **Distributed Acoustic Sensing (DAS) of Seismic Properties in a Borehole**  
2                           **drilled on a Fast-Flowing Greenlandic Outlet Glacier**

3  
4 Adam D Booth<sup>1</sup>, Poul Christoffersen<sup>2</sup>, Charlotte Schoonman<sup>2</sup>, Andy Clarke<sup>3</sup>, Bryn Hubbard<sup>4</sup>,  
5 Rob Law<sup>2</sup>, Samuel H Doyle<sup>4</sup>, Tom R Chudley<sup>2</sup>, Athena Chalari<sup>3</sup>

6  
7 1. Institute of Applied Geoscience, School of Earth and Environment, University of Leeds, LS2  
8 9JT, UK.

9 2. Scott Polar Research Institute, Department of Geography, University of Cambridge, Lensfield  
10 Road, Cambridge, CB2 1ER, UK.

11 3. Silixa Ltd, Silixa House, 230 Centennial Park, Centennial Avenue, Elstree, Wd6 3SN, UK

12 4. Centre for Glaciology, Department of Geography and Earth Sciences, Aberystwyth  
13 University, Aberystwyth, SY23 3DB, UK

14  
15 Corresponding author: Adam Booth ([a.d.booth@leeds.ac.uk](mailto:a.d.booth@leeds.ac.uk))

16  
17 **Key Points:**

- 18       • Distributed Acoustic Sensing (DAS) is a novel seismic surveying technology which uses  
19       fibre-optic cables to record seismic energy.
- 20       • We present the first glaciological application of DAS, installing cable in a 1030 m-long  
21       borehole drilled on Greenland's Store Glacier.
- 22       • We evidence, at 10 m vertical resolution, anisotropic and temperate ice beyond ~850 m  
23       depth and ~20 m of consolidated subglacial sediment.

24  
25

**Abstract**

Distributed acoustic sensing (DAS) is a new technology in which seismic energy is recorded at high spatial and temporal resolution along a fibre-optic cable. We show analyses from the first glaciological borehole deployment of DAS to measure the englacial and subglacial seismic properties of Store Glacier, a fast-flowing outlet of the Greenland Ice Sheet. By characterizing compressional and shear wave propagation in 1030 m-deep vertical seismic profiles, sampled at 10 m vertical resolution, we detected a transition from isotropic to anisotropic ice consistent with a Holocene-Wisconsin transition at 83% of the ice thickness. We also infer temperate ice in the lowermost 100 m of the glacier, and identified subglacial reflections originating from the base of a 20 m-thick layer of consolidated sediment. Our findings highlight the transformative potential of DAS to inform the physical properties of glaciers and ice sheets.

37

**Plain Language Summary**

The seismic properties of glaciers and ice masses have a fundamental influence on ice flow, and help inform predictive models of how ice dynamics will evolve. Distributed acoustic sensing (DAS) is a revolutionary technology for seismic surveying, in which fibre-optic cables are used to record seismic waves with unprecedented resolution. Our paper presents data from the first glaciological deployment of a DAS system which we installed in a 1030 m-deep vertical borehole on Store Glacier, a fast-flowing outlet of the Greenland Ice Sheet. The detailed seismic anatomy of the glacier that our survey provides – an independent measurement of the seismic response every 10 m – gives new insights about its internal flow regime and temperature, and even allows us to detect layers of sediment underlying it. We predict that DAS surveying will play an increasingly large role in future glaciological seismic surveys as the recognition of its transformative potential grows.

50

51

52

53

54 **1. Introduction**

55 Seismic methods are widely applied in glaciology to quantify the englacial and basal properties  
56 of ice masses. Seismic velocity variations can indicate the strength and style of ice crystal fabrics  
57 (e.g., Diez et al., 2015; Smith et al., 2017; Brisbourne et al., 2019) and quantify intracrystalline  
58 water and debris (Hauck et al., 2011). Seismic attenuation rates vary with englacial temperature  
59 (Peters et al., 2012), and seismic reflectivity helps constrain the composition of subglacial  
60 material (e.g., Anandakrishnan, 2003; Dow et al., 2013). Combined estimates of compressional  
61 (P-) and shear (S-) wave velocities yield mechanical properties such as Poisson's ratio and  
62 bulk/shear moduli (e.g., Polom et al., 2013; Kulesa et al., 2019).

63 Most glaciological seismic acquisitions install receivers at, or close to, the glacier surface.  
64 Although logistically practical, quantitative interpretations of the resulting data make numerous  
65 assumptions about seismic propagation. Velocities derived from englacial or basal reflections  
66 typically make hyperbolic travel-time approximations, and estimates of physical properties  
67 (internal layering or e.g., bed reflectivity) must compensate for propagation processes between  
68 the source, the target and receivers. Although a paucity of ground-truth data can be mitigated  
69 using data-driven corrections (e.g., King et al., 2008; Peters et al., 2008, 2012), derivations of  
70 seismic quantities often remain under-constrained. The problem is exacerbated for passive  
71 seismic datasets, where source positions are unknown and location algorithms must assume  
72 background velocity/attenuation structures (e.g., Rösli et al., 2014; Podolskiy and Walter,  
73 2016).

74 Borehole seismic deployments are advantageous because they (i) enable calibration of surface  
75 seismic responses and (ii) sample and provide local *in situ* seismic quantities. Data interpretation  
76 using a 'vertical seismic profile' (VSP) geometry invokes fewer travel-time assumptions than the  
77 surface seismic case, improving the accuracy of local seismic property estimates. These  
78 properties can extend to velocity and velocity anisotropy (Diez et al., 2015), attenuation  
79 (Beckwith et al., 2017) and reflection coefficient (Lira et al., 2012). Furthermore, VSP surveying  
80 offers a measurement of englacial seismic properties even for homogeneous ice columns that  
81 feature no internal reflectivity.

82 Seismic studies have benefited from the recent development of distributed acoustic sensing  
83 (DAS). DAS systems involve sending laser pulses into a fibre-optic cable from an *interrogator*  
84 unit. As they travel, a fraction of these pulses is backscattered via Rayleigh scattering, with the  
85 phase-lag in the backscattered pulse changing as the cable is strained, e.g., by the passage of  
86 seismic wavelets. Phase-lags are measured by the interrogator and used to simultaneously  
87 reconstruct the seismic response along the cable (Hartog et al., 2013). A length of fibre-optic  
88 cable therefore acts as a continuous geophone string. Besides their interpretative potential, DAS  
89 methods are logistically attractive in glaciology; e.g., conventional borehole seismic instruments  
90 may be lost in deforming/freezing boreholes, whereas DAS cables are designed to freeze in place  
91 even if they ultimately snap under englacial strain. As with conventional geophones, DAS  
92 systems can record in active and passive modes, enabling glacier seismicity to be monitored at  
93 high temporal and vertical resolution. DAS VSP datasets therefore offer powerful potential for *in*  
94 *situ* monitoring of englacial seismic properties.

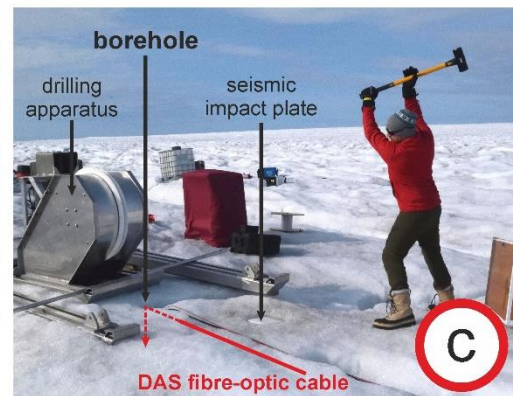
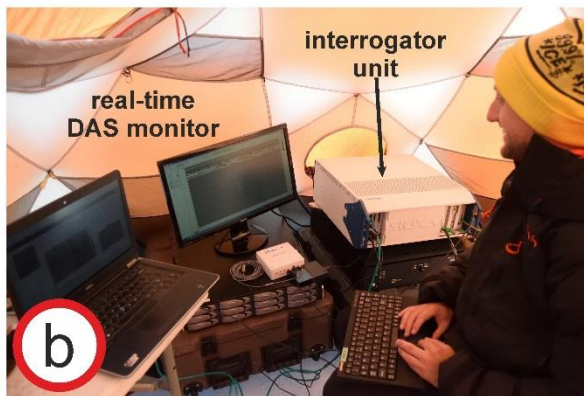
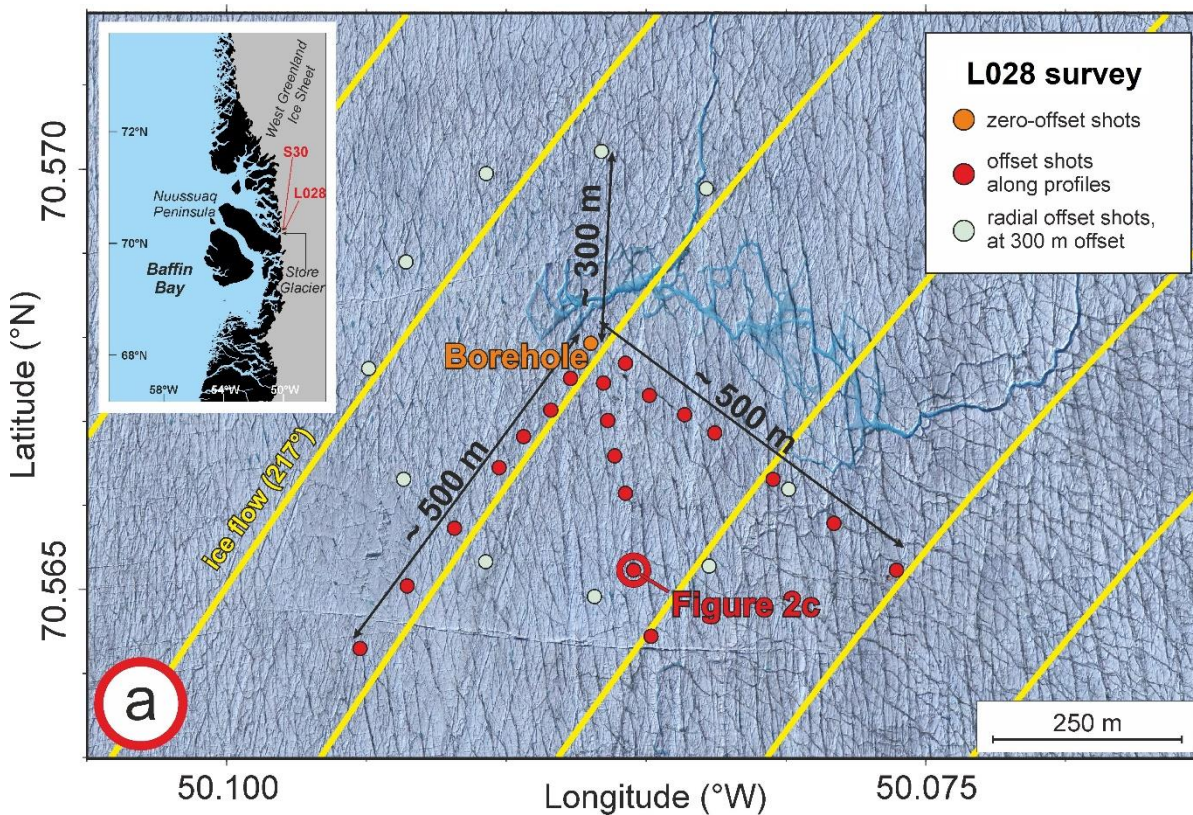
95 Here, we interpret data from the first deployment of DAS technology within a glacier borehole.  
96 The survey was performed during the summer of 2019 on fast-flowing Store Glacier in West  
97 Greenland. We highlight the scope of the VSP DAS dataset, determining i) the vertical P-wave  
98 velocity and attenuation structure of the ice column, ii) Poisson's ratio using combined P- and S-  
99 wave arrivals, and ii) seismic properties and thickness of subglacial sediment layers.

## 100 **2. Field setting and deployment**

101 Store Glacier (Greenlandic: *Sermeq Kujalleq*) is a marine-terminating outlet glacier that drains  
102  $\sim 34,000$  km<sup>2</sup> of the Greenland Ice Sheet, and flows into Uummannaq Fjord (Rignot et al., 2008).  
103 Previously, the subglacial environment of the glacier was targeted at site S30 (inset, Figure 1)  
104 with boreholes drilled by pressurised hot water. Here, flow speeds of 600 m a<sup>-1</sup> occur in response  
105 to high basal water pressure (Doyle et al., 2018) over a sedimentary bed (Hofstede et al., 2018).

106 In July 2019, boreholes were drilled in the centre of supraglacial lake site L028 (70.56793°N  
107 50.08697°W; Figure 1), which drained via hydrofracture on 31 May 2019 (Chudley et al., 2019).  
108 A vertical borehole was instrumented with a Solifos BRUsens fibre-optic cable, installed to  
109  $\sim 1030$  m depth; the rapid loss of borehole water into a basal hydrological system confirms that  
110 the borehole, and therefore the cable, terminates at the glacier bed. The cable contained two

111 single-mode fibres (for DAS) and four multi-mode fibres (for distributed temperature sensing,  
 112 DTS, to be reported elsewhere), enclosed in a gel-filled stainless-steel capillary tube, with 4.8  
 113 mm-diameter polyamide sheathing and steel wire reinforcement. DAS VSPs were then recorded  
 114 during a 3-day period, between 6-8 July 2019.



115  
 116 Figure 1. a) Location of seismic shots (red, grey) around the L028 borehole (orange); yellow  
 117 lines denote ice flow. Inset: Sites S30 and L028 in West Greenland. b) Silixa iDAS™  
 118 interrogator and acquisition monitor. c) Zero-offset VSP hammer shot.

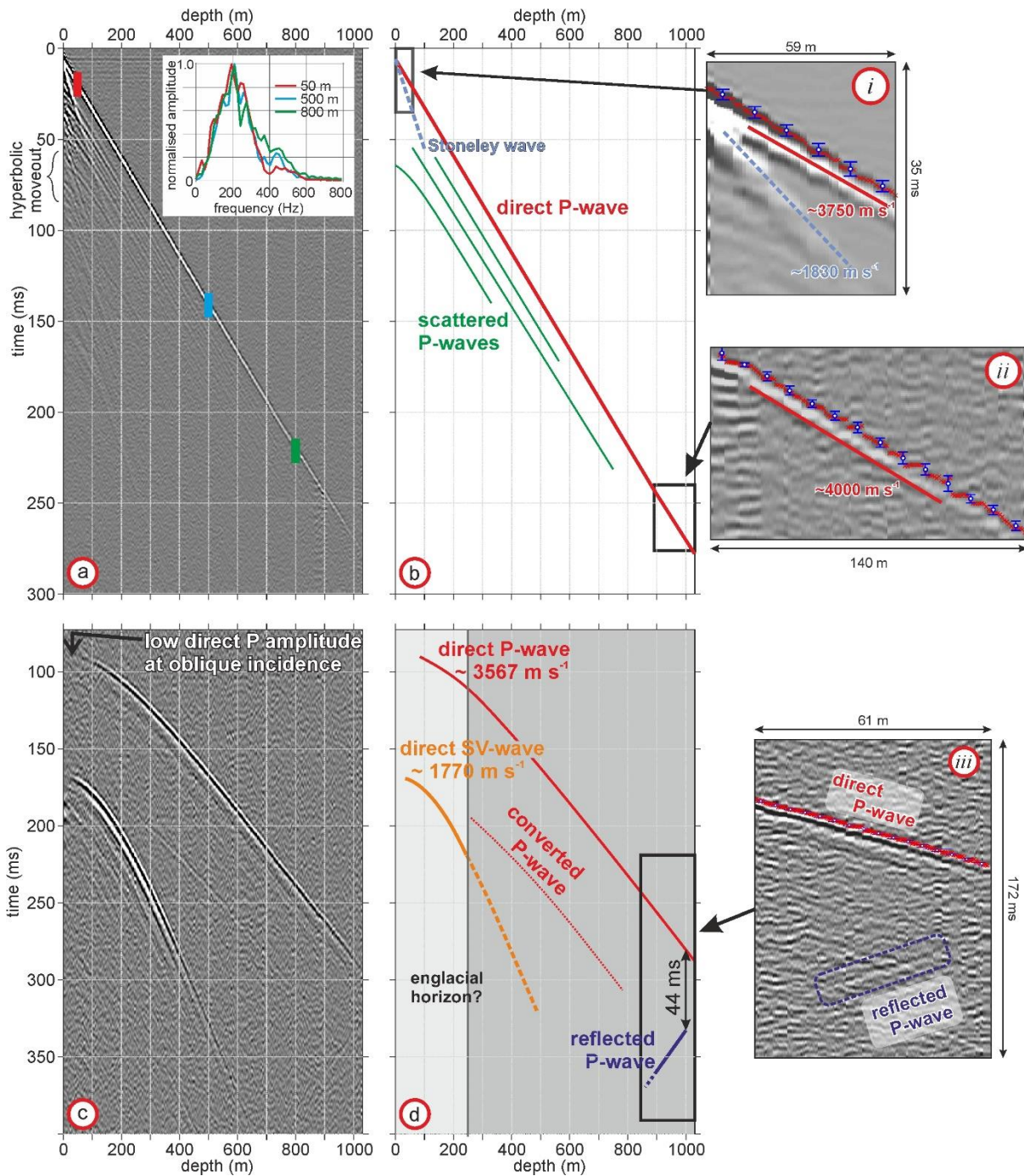
119 A Silixa iDAS<sup>TM</sup> interrogator (Figure 1b), recording at 4000 Hz sampling frequency, established  
120 the seismic response every 1 m along the cable. However, the effective resolution of the  
121 acquisition is 10 m because the backscattered phase-lag is measured over a ~10 m ‘gauge  
122 length’. Cable sensitivity varies as a function of the incidence angle,  $\theta$ , of seismic energy to the  
123 cable axis, as  $\cos^2\theta$  for P-waves and  $\sin^2\theta$  for vertically-polarized shear (SV-) waves (Mateeva *et*  
124 *al.*, 2014). The system is insensitive to horizontally-polarized shear (SH-) waves. For the vertical  
125 installation reported here, the cable is most sensitive to vertically-propagating P-waves, and  
126 insensitive to those travelling horizontally. The converse holds for SV-waves.

127 Seismic energy was generated with a 7 kg sledgehammer striking a polyethylene impact plate  
128 (dimensions 0.20x0.20x0.05 m). Shots were made (i) ~1 m away from the borehole top  
129 (effectively zero-offset; Figure 1c), (ii) along azimuths parallel, orthogonal and at 45° to ice flow  
130 (~217°), up to 500 m offset from the borehole, and (iii) radially, at 30° intervals, at 300 m  
131 nominal offset from the borehole. For stacking, ~30 hammer strikes were recorded at each  
132 location over a ~4 minute period. Recorded seismic wavelets were consistent, and the  
133 typical correlation coefficient between successive traces in a shooting sequence is >0.96).

134 The fibre-optic cable was monitored in a passive mode. Zero-offset shots were extracted from  
135 the record by identifying the earliest arrival of seismic energy at the approximate time of  
136 shooting. For offset shooting, impact times were recorded with a GPS-synchronized surface  
137 geophone installed within 1 m of the impact place, and later used to extract data from the passive  
138 DAS record. These times are typically accurate to  $\pm 1$  ms; residual static corrections, typically  
139  $< \pm 0.75$  ms, were applied to synchronize shots prior to stacking.

### 140 **3. VSP Data**

141 Two VSPs are shown (Figure 2), acquired with zero-offset (2a,b) and offset (2c,d) geometries,  
142 on 7 July 2019 (12:15 and 20:00 UTC respectively). The source in the offset VSP is located  
143 306.4 m south of the borehole (see Figure 1), hereafter termed ‘300 m offset’. Prominent arrivals  
144 are annotated for each record, together with initial velocity assessments. The enlarged panels in  
145 Figure 2b show direct-wave first-break picks for each trace (red crosses) and the mean and  
146 standard deviation of these within each 10 m gauge length (blue symbols). VSP acquisition  
147 geometries are described in the Supporting Information.



148

149 Figure 2. a) Zero-offset VSP; inset, amplitude spectra at 50 (red), 500 (blue) and 800 m (green)  
 150 depths. b) Identification of arrivals in (a). c) 300 m offset VSP. d) Identification of arrivals in (c).  
 151 Panels *i-iii* show enlarged sections of VSP data; red crosses show first-break picks, and blue  
 152 symbols show their mean and standard deviation across a gauge length (blue).

153

### 154 3.1 Zero-offset VSP

155 The dominant arrival in the zero-offset record is the direct P-wave (Figure 2b), with linear  
156 moveout and no abrupt gradient changes, hence suggesting no strong englacial P-wave velocity  
157 ( $v_P$ ) contrasts. However, linear trends fitted in shallow and deep intervals suggest a subtle  $v_P$   
158 increase with depth:  $\sim 3750 \text{ m s}^{-1}$  in the upper 50 m, versus  $\sim 4000 \text{ m s}^{-1}$  in the lowermost 150 m  
159 (panels *i*, *ii*). The direct wave amplitude spectrum is stable throughout the VSP, with a dominant  
160 frequency of  $\sim 200 \text{ Hz}$  and a bandwidth of  $\sim 200 \text{ Hz}$  (inset, Figure 2a). The absence of a basal  
161 reflection at 1030 m depth is consistent with the low-reflectivity bed observed previously but, is  
162 consistent with low-reflectivity bed conditions observed previously (Hofstede et al., 2018).

163 Events that parallel the direct wave are interpreted as P-wave energy backscattered from, e.g.  
164 surface crevasses. In the upper 100 m of the VSP, between 50 and 70 ms, these arrivals have  
165 hyperbolic moveout, consistent with an origin offset from the borehole top. The linear arrival  
166 following the direct wave has a velocity of  $\sim 1830 \text{ m s}^{-1}$ , close to the typical S-wave velocity ( $v_S$ )  
167 in ice. This arrival is interpreted as a Stoneley wave (Cheng and Toksöz, 1981), a vertically-  
168 travelling phase that propagates at a solid-solid interface, assumed to be the refrozen borehole  
169 wall.

### 170 3.2 300 m offset VSP

171 The offset VSP features a prominent hyperbolic direct P-wave (Figure 2c), detectable only below  
172  $\sim 70 \text{ m}$  given the near-perpendicular arrivals at such shallow depths. The best-fit hyperbola to the  
173 upper 200 m of direct P-wave travel-times gives  $v_P$  of  $3567 \pm 7 \text{ m s}^{-1}$  (Figure 2d). The later  
174 hyperbolic event (zero-depth arrival time  $\sim 160 \text{ ms}$ ) is the direct SV-wave and its best-fit  
175 hyperbola defines  $v_S$  of  $1770 \pm 2 \text{ m s}^{-1}$  for the upper 200 m. SV-wave amplitudes decay rapidly  
176 with depth due to combined propagation losses and cable sensitivity. Neither arrival shows an  
177 abrupt change in curvature, although a P-wave trend appears to diverge from the direct SV-wave  
178 from depths  $> 250 \text{ m}$ . This is interpreted as a SV-to-P mode conversion, and requires there to be a  
179 horizon around 250 m depth. This must represent a subtle change in P- and SV-wave velocities  
180 to suppress reflectivity but offers a strong velocity increase from SV- to P- propagation, given  
181 that compressional waves typically travel 2-times faster in ice than shear.

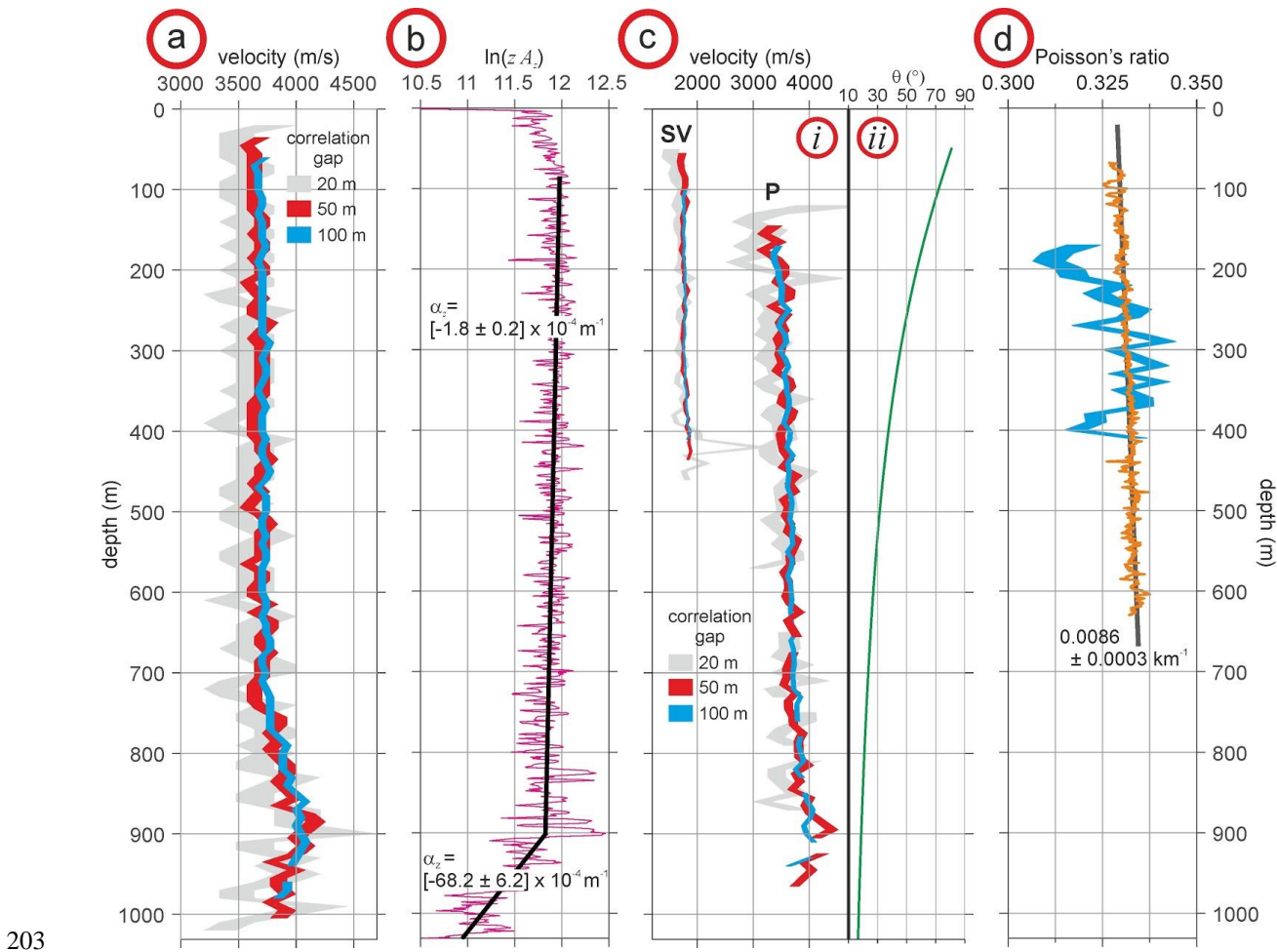
182 Consistent with the zero-offset VSP, there is no apparent P-wave basal reflection, but a low-  
183 amplitude reflection *is* still visible in the lowermost 150 m (panel *iii*). This event does not  
184 converge on the direct wave but, at the deepest point that it is visible (~990 m), lags it by ~44  
185 ms. Since the borehole terminates at the glacier bed, at 1030 m, this reflection must originate  
186 subglacially, propagating through a velocity:thickness model that defines a ~44 ms two-way  
187 travel-time.

## 188 **4. Quantitative VSP Interpretation**

### 189 4.1 Vertical velocity model

190 Owing to the vertical cable and wave propagation,  $v_P$  in any depth interval is the depth difference  
191 between two observation points, divided by the travel-time of energy between them. We  
192 calculate travel-times by cross-correlating traces from different depth intervals and recording the  
193 time-lag of the cross-correlation peak. Thus, the velocity obtained is the average P-wave interval  
194 velocity within the correlation gap, with longer gaps increasing the degree of vertical smoothing.

195 Vertical  $v_P$  trends are estimated for correlation gaps of 20, 50 and 100 m (grey, red, blue,  
196 respectively, in Figure 3a). The 20 m gap offers high vertical resolution but is noisy since errors  
197 in identifying the cross-correlation lag ( $\pm 1$  digital sample, = 0.25 ms) are a greater proportion of  
198 the interval travel-time. Both 50 and 100 m trends show constant  $v_P$  of  $3700 \pm 70 \text{ m s}^{-1}$  in the  
199 upper 800 m, rising to  $4100 \pm 70 \text{ m s}^{-1}$  between 800 and 900 m depth, and decreasing to  $3850 \pm 70$   
200  $\text{m s}^{-1}$  in the lowermost 100 m. Curve widths represent the velocity uncertainty from  
201 misidentifying the peak cross-correlation lag by  $\pm 0.25$  ms, but the trend is evident regardless of  
202 these errors or the correlation gap hence is considered as a genuine velocity feature.



203

204 Figure 3. a) Depth variation of vertical  $v_P$ , estimated using VSP cross-correlation gaps of 20 m  
 205 (grey), 50 m (red) and 100 m (blue). Curve width relates to  $\pm 0.25$  ms error in identifying cross-  
 206 correlation peaks. b) Amplitude decay attributable to anelastic attenuation. Black lines show  
 207 best-fit linear trends in intervals 85 to 900 m, and 900 to 1030 m. c) As (a), but showing  $v_P$  and  
 208  $v_S$  derived from the 300 m offset VSP (i). Green trend in (ii) shows the incidence angle,  $\theta$ , of  
 209 direct waves to the cable axis. d) Local variation of Poisson's ratio (blue), and the raypath-  
 210 averaged Poisson's ratio trend (orange).

211

## 212 4.2 Vertical attenuation model

213 The amplitude,  $A_x$ , of a seismic wave decreases with propagation due to geometric spreading and  
 214 anelastic attenuation losses, expressed as:

215 
$$A_x = A_0 G(x) e^{-\alpha x} \tag{1}$$

216 where  $A_0$  is initial amplitude,  $G(x)$  is geometric spreading losses,  $\alpha$  is an attenuation coefficient  
 217 and  $x$  is the distance travelled. For the zero-offset VSP, this distance is the depth,  $z$ , of the  
 218 observation point along the fibre-optic cable, hence  $G(x)$  varies as  $z^{-1}$ . Therefore, on rearranging  
 219 Equation (1) as

220 
$$\alpha_z = -z \ln \left( \frac{z A_z}{A_0} \right), \tag{2}$$

221 the gradient in a plot of  $z$  against  $\ln \left( \frac{z A_z}{A_0} \right)$  defines the depth-averaged attenuation coefficient,  $\alpha_z$ .

222 The P-wave attenuation coefficient is related, via  $v_P$ , to the seismic quality factor,  $Q$ , by

223 
$$Q = \frac{-\pi f}{v_P \alpha_z}, \tag{3}$$

224 where  $f$  is wavelet frequency.  $Q$  has been related to englacial temperature (Peters et al., 2012),  
 225 with warmer ice associated with lower- $Q$  values and therefore increased attenuation. Peters et al.  
 226 (2012) measure  $Q$  from englacial reflections using spectral ratios (Dasgupta and Clark, 1998). In  
 227 our data, the consistency of spectra (Figure 2a) suggests that  $Q$  is high and spectral ratios could  
 228 be influenced more by noise than genuine attenuation signatures. We therefore measure  $\alpha_z$ , and  
 229 therefore  $Q$ , from the amplitude decay of the direct P-wave.

230 Following corrections for spreading losses and assuming  $A_0 = 1$ , the depth variation of direct  
 231 wave amplitudes (Figure 3b) has three linear sections. The increase of amplitude to ~85 m depth  
 232 is non-physical and attributed to interference with the Stoneley wave. Between 85 and 900 m,  
 233 amplitudes decay linearly and imply  $\alpha_z$  of  $[-1.8 \pm 0.2] \times 10^{-4} \text{ m}^{-1}$ . For the lowest ~100 m,  $\alpha_z$  is  $[-$   
 234  $68.2 \pm 6.2] \times 10^{-4} \text{ m}^{-1}$ . Assuming the  $v_P$  derived previously and a dominant wavelet frequency  
 235 of 200 Hz, Equation 3 implies  $Q_{200}$  of  $925 \pm 120$  and  $24 \pm 3$  respectively in these intervals.

236 **4.3 Shear wave velocity and Poisson's ratio**

237 Poisson's ratio describes how a material deforms when under stress, specifically the ratio of  
 238 transverse extension to axial compression. In ice, Poisson's ratio is typically 0.3-0.34 (Köhler et

239 al., 2019) but is sensitive to the strength of anisotropy (Nanthikesan and Shyam Sunder, 1994)  
 240 and shows some tendency to increase with temperature (Weeks and Assur, 1967).

241 The dynamic Poisson's ratio,  $\nu_d$ , is defined using  $\nu_P$  and  $\nu_S$  as:

$$242 \quad \nu_d = \frac{(v_P/v_S)^2 - 2}{2[(v_P/v_S)^2 - 1]}. \quad (4)$$

243 The variation of  $\nu_P$  and  $\nu_S$  (Figure 3*ci*) is measured from the offset VSP following the same  
 244 cross-correlation procedure applied to the zero-offset data. However, since direct waves in the  
 245 offset VSP arrive at an oblique angle  $\theta$  to the cable axis (Figure 3*c*, inset *ii*), path length  
 246 differences must be modified by the mean  $\cos\theta$  within any given depth interval. These estimates  
 247 neglect refraction effects (i.e., assume straight rays), but this is reasonable given the constant  
 248 velocities observed through much of the ice column.

249 P-wave velocities are consistent with those in Figure 3*a*, including the velocity variation in the  
 250 lowermost 200 m. An increase in  $\nu_P$  with depth is possible, potentially due to anisotropy or as an  
 251 adverse consequence of assuming straight rays. Between 100-300 m,  $\nu_S$  is  $\sim 1740 \pm 20 \text{ m s}^{-1}$ , and  
 252 increases to  $\sim 1850 \pm 20 \text{ m s}^{-1}$  at 450 m depth, albeit with the same straight-ray caveat.

253 Figure 3*d* shows two measures of Poisson's ratio. The first (orange curve) is path-averaged;  
 254 under the straight-ray assumption, direct P- and SV-waves follow the same path, hence the ratio  
 255  $\nu_P/\nu_S$  is equivalent to the ratio of SV-to-P first-break travel-times. The mean Poisson's ratio  
 256 recorded is  $0.332 \pm 0.002$ , but this increases by  $0.0086 \pm 0.0003 \text{ km}^{-1}$  over the interval 80 to 620  
 257 m. The second measure is the discretized Poisson's ratio, estimated using  $\nu_P$  and  $\nu_S$  obtained for  
 258 the 100 m correlation gap (thus limiting its evaluation to depths with mutual P and SV coverage).  
 259 For this second case, Poisson's ratio increases to  $\sim 250$  m depth, beyond which the mean value  
 260 stabilizes at  $0.331 \pm 0.007$ . Although the measurement of Poisson's ratio is smoothed over a 100  
 261 m interval, this depth is consistent with the apparent position of the mode-converting horizon  
 262 apparent in Figure 2*d*, hence a transition in ice properties is inferred around this depth. In future  
 263 analyses, the validity of these trends and the implied mode conversion will be explored using  
 264 more sophisticated ray-tracing algorithms.

265

266 4.4 Thickness modelling of subglacial layering

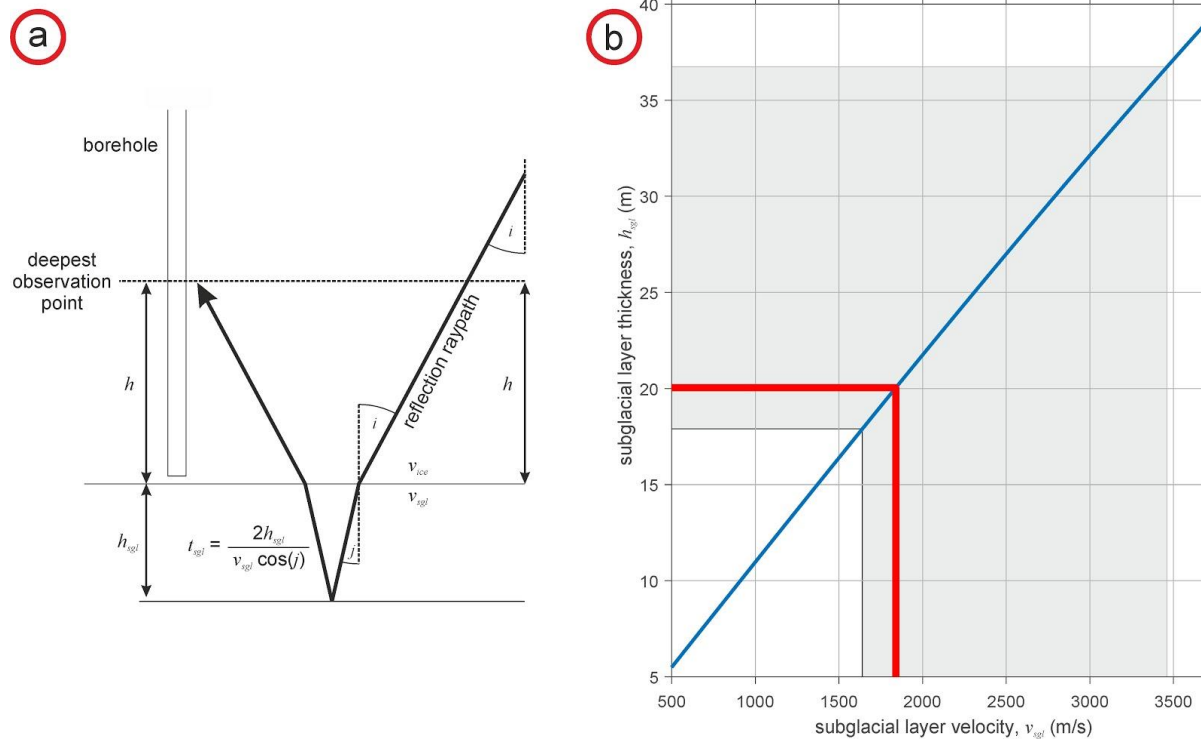
267 Although the P-wave velocity and thickness of layering beneath the borehole cannot be  
 268 determined uniquely, permissible  $v_P$ :thickness pairs satisfy a 44 ms two-way travel-time (Figure  
 269 2d). However, the deepest depth at which the reflection can reliably be perceived is 990 m,  
 270 meaning 40 m of one-way propagation must be in basal ice. The travel-time contribution of the  
 271 ice leg,  $t_{ice}$ , is

$$272 \quad t_{ice} = \frac{2h}{v_{ice}\cos(i)} \quad (5)$$

273 where  $h$  is the distance above the glacier bed,  $v_{ice}$  is velocity through ice and  $i$  is the angle of  
 274 incidence to the vertical (Figure 4a). For the offset VSP geometry,  $i$  is  $\sim 17^\circ$  and  $v_{ice}$  is  $3850 \text{ m s}^{-1}$   
 275 (Figure 3). Therefore, Equation 5 shows that 22 ms of the 44 ms round-trip comprises  
 276 propagation through ice, with the remaining 22 ms being travel-time through the subglacial  
 277 layer,  $t_{sgl}$ . The thickness of this layer,  $h_{sgl}$ , is

$$278 \quad h_{sgl} = \frac{1}{2}v_{sgl}t_{sgl}\cos(j), \quad (6)$$

279 where  $v_{sgl}$  is the subglacial layer velocity and  $j$  is the refracted angle into the subglacial layer  
 280 (from Snell's law,  $j = v_{sgl} \cos(i)/v_{ice}$ ). Equation 6 assumes a horizontal subglacial reflector,  
 281 and negligible difference in incidence angles for the direct wave and the downgoing reflection  
 282 leg ( $\sim 0.6^\circ$  for our geometry). The blue curve in Figure 4b shows pairs of  $v_{sgl}$  and  $h_{sgl}$  that  
 283 satisfy  $t_{sgl} = 22 \text{ ms}$ . Hofstede et al. (2018) gave  $v_P$  of  $1839^{+1618}_{-94} \text{ m s}^{-1}$  for subglacial material  
 284 beneath site S30; assuming the same velocity at L028,  $h_{sgl}$  is  $20^{+17}_{-2} \text{ m}$ .



285

286 Figure 4. a) Schematic representation of Equations 5 and 6. b) Thickness estimation of subglacial  
 287 layering, for  $v_{sgl}: h_{sgl}$  pairs that satisfy  $t_{sgl} = 22$  ms. The grey shading shows the  $v_{sgl}$  range  
 288 constrained for Store Glacier by Hofstede et al. (2018) and its corresponding  $h_{sgl}$ , with the red  
 289 line showing  $h_{sgl}$  for their preferred velocity of  $1839 \text{ m s}^{-1}$ .

290

## 291 5. Discussion and conclusions

### 292 5.1 VSP analyses

293 The zero-offset VSP shows little  $v_P$  variation through the upper 800 m of Store Glacier, but  
 294 increases to  $\sim 4100 \pm 70 \text{ m s}^{-1}$  at  $\sim 850$  m depth. This velocity is consistent with P-wave energy  
 295 travelling vertically through anisotropic ice with a  $0^\circ$  cone opening angle (Diez et al., 2015). In  
 296 our data, the transition to an anisotropic fabric appears gradational, attributable either to the  
 297 vertical smoothing we apply or to a genuinely smooth transition that can only be detected given  
 298 the finer vertical sampling provided by DAS recording. At site S30, Hofstede et al. (2018)  
 299 detected an anisotropic transition in the lowermost  $\sim 80$  m of Store Glacier, consistent with

300 deformation recorded in the lowermost 100 m of the ice (Doyle et al., 2018), and interpreted it as  
301 the transition from Holocene- to Wisconsin-age ice (HWT). Our data suggest that the HWT  
302 beneath L028 is located at ~850 m depth, ~83% of ice thickness, matching reported estimates of  
303 82-85% (Karlson et al., 2013).

304 Attenuation rates are low throughout most of the ice column, implying efficient propagation  
305 through cold ice, but increase by  $>2$  orders of magnitude in the lowermost ~100 m. At these  
306 depths, we measure  $Q_{200}$  of  $24 \pm 3$ , similar to values measured by Peters et al. (2012) for  
307 temperate ice ( $\sim -1$  °C) at the base of Greenland's Jakobshavn Isbrae. We therefore predict  
308 similar conditions in the lowermost ice of Store Glacier. To what extent the  $v_p$  reduction in the  
309 lowermost 50 m of the ice column is related to temperate ice versus weaker anisotropy will be  
310 explored alongside co-located DTS records.

311 The offset VSP allowed constraint of both P- and SV- wave properties. Although englacial  
312 velocity contrasts were not detectable for either direct wave, a horizon appears to be present at  
313 ~250 m depth to convert SV- to P- wave energy. This may be associated with an increase in  
314 Poisson's ratio, implying that the underlying ice is more deformable; again, DTS measurements  
315 will be used to investigate englacial temperatures at this depth.

316 Subglacial reflections were observed, originating beyond the borehole termination from the base  
317 of a layer that is  $20_{-2}^{+17}$  m thick. Since the glacier bed has low reflectivity, the acoustic  
318 impedance of subglacial material must balance that of the basal ice ( $\sim 3.5 \times 10^6 \text{ kg m}^{-2} \text{ s}^{-1}$ ). With  
319  $v_{sgl} = 1839 \text{ m s}^{-1}$ , the impedance contrast would be removed if the density of subglacial material  
320 was  $\sim 1900 \text{ kg m}^{-3}$ . Considering the elastic properties tabulated in Christianson et al. (2014), this  
321 density implies that site L028 is underlain by consolidated, but neither deforming nor lithified,  
322 sediment.

## 323 5.2 DAS applicability

324 DAS methods are clearly beneficial for characterizing the seismic properties of ice masses at  
325 high resolution. Nonetheless, vertically-orientated fibre-optic cables are limited by their  
326 insensitivity to oblique particle motion; a well-coupled three-component geophone would record  
327 all senses of particle motion, including SH-waves that are undetectable with DAS. However, the

328 ability of DAS to reconstruct independent seismic responses every ~10 m throughout the ice  
329 column can outweigh these shortcomings, particularly if the goal of the survey is to benchmark  
330 P-wave properties for conventional surface seismic analysis.

331 Our DAS cable has limited applicability as a horizontally-oriented receiver for surface-seismic  
332 surveying. Basal reflections would arrive with near-vertical incidence at the surface, hence with  
333 particle motion orthogonal to the cable axis. Considering Figures 2c and 3cii, in which P-wave  
334 arrivals appear undetectable beyond ~70° incidence, reflections from a 1 km-deep target would  
335 only be detected at offsets >600 m. The recent development of *helically-wound* fibre-optic cables  
336 (Kuvshinov, 2015), sensitive to all directions of particle motion, could mitigate such limitations.

337 From a logistical perspective, once installed in a borehole, DAS recording is less challenging  
338 than, e.g., deploying downhole source or receiver tools. Such tools risk being frozen in place,  
339 hence must be used quickly and/or with compromised spatial sampling regimes.

### 340 5.3 Conclusions

341 We have demonstrated the feasibility and value of DAS surveying in glaciology. Our VSP  
342 acquisitions sample the seismic response, at 10 m vertical resolution, throughout the 1030 m  
343 thickness of a fast-flowing glacier in Greenland. These experiments allowed us to (i) measure the  
344 variation of P- and SV-wave properties, (ii) detect transitions relating to ice crystal fabric and  
345 temperature regimes in the lowermost 150 m of the glacier, and (iii) identify a subglacial layer of  
346 consolidated sediment up to 40 m thick. Extended analyses of these data will consider the  
347 azimuthal variation of the seismic response and the passive observations of natural seismicity  
348 around the L028 site, in conjunction with co-located pRES and DTS measurements.

349 We believe that DAS surveys will play an increasingly important role in glacier seismology, both  
350 in passive- and active-source modes, as the increasing recognition of the technique's potential  
351 increases.

352

353

354

## 355 Acknowledgements

356 The authors declare no financial conflict of interest. This research was funded by the European  
357 Research Council as part of the RESPONDER project under the European Union's Horizon2020  
358 research and innovation program (Grant 683043). BH was supported by a HERCW /  
359 Aberystwyth University Capital Equipment Grant. TRC and RL are supported by Natural  
360 Environment Research Council Doctoral Training Partnership studentships (grant  
361 NE/L002507/1). VSP stacking was performed by Diana Rosado (University of Leeds MSc  
362 Exploration Geophysics), and attenuation analyses benefitted from constructive discussions with  
363 Roger Clark.

364 Supporting data will be uploaded, following best practice, to a figshare repository. These will be  
365 the two VSP datasets presented in Figure 2.

366

## 367 References

368 Aki, K., & Richards, P.G. (2002), *Quantitative Seismology*, 2<sup>nd</sup> edition, University Science  
369 Books, Sausalito, California.

370 Anandkrishnan, S. (2003), Dilatant till near the onset of streaming flow of Ice Stream C, West  
371 Antarctica, determined by AVO (amplitude vs offset) analysis. *Annals of Glaciology*, 36, 283-  
372 286. doi: 10.3189/172756403781816329.

373 Beckwith, J., Clark, R. & Hodgson, L. (2017), Estimating frequency-dependent attenuation  
374 quality factor values from prestack surface seismic data. *Geophysics*, 82(1), O11-O22. doi:  
375 10.1190/geo2016-0169.1

376 Brisbourne, A.M., Martín, C., Smith, A.M., Baird, A., Kendall, J.M. & Kingslake, J. (2019),  
377 Constraining recent ice flow history at Korff Ice Rise, West Antarctica, using radar and seismic  
378 measurements of ice fabric. *Journal of Geophysical Research: Earth Surface*, 124(4851). doi:  
379 10.1029/2018JF004776.

380 Cheng, C.H. & Toksöz, M.N. (1981), Elastic wave propagation in fluid-filled borehole and  
381 synthetic acoustic logs. *Geophysics*, 46, 1042-1053. doi: 10.1190/1.1441242.

- 382 Christianson, K., Peters, L.E., Alley, R.B., Anandakrishnan, S., Jacobel, R.W., Riverman, K.L.,  
383 Muto, A. & Keisling, B.A. (2014), Dilatant till facilitates ice-stream flow in northeast Greenland.  
384 *Earth and Planetary Science Letters*, 410, 57-69. doi: 10.1016/j.espl.2104.05.060.
- 385 Chudley, T.R., Christoffersen, P., Doyle, S.H., Bougamont, M., Schoonman, C.M., Hubbard, B.  
386 & James, M.R. (2019), Supraglacial lake drainage at a fast-flowing Greenlandic outlet glacier,  
387 *Proceedings of the National Academy of Sciences*, 116 (51), 25468-25477. doi:  
388 10.1073/pnas.1913685116.
- 389 Dasgupta, R. & Clark RA (1998), Estimation of  $Q$  from surface seismic reflection data,  
390 *Geophysics*, 63(6), 2120-2128. doi: 10.1190/1.1444505.
- 391 Diez, A., Eisen, O., Hofstede, C., Lambrecht, A., Mayer, C., Miller, H., Steinhage, D., Binder, T.  
392 & Weikusat, I. (2015), Seismic wave propagation in anisotropic ice - Part 2: Effects of crystal  
393 anisotropy in geophysical data, *The Cryosphere*, 9, 385-398. doi: 10.5194/tc-9-385.2015.
- 394 Dow, C.F., Hubbard, A., Booth, A.D., Doyle, S.H., Gusmeroli, A. & Kulesa, B. (2013), Seismic  
395 evidence of mechanically weak sediments underlying Russell Glacier, West Greenland, *Annals*  
396 *of Glaciology*, 54(64), 135-141. doi: 10.3189/2013AoG64A032.
- 397 Doyle, S.H., Hubbard, B., Christoffersen, P., Young, T.J., Hofstede, C., Bougamont, M., Box,  
398 J.E. & Hubbard, A. (2018), Physical conditions of fast glacier flow: 1. Measurements from  
399 boreholes drilled to the bed of Store Glacier, West Greenland, *Journal of Geophysical Research:*  
400 *Earth Surface*, 123, 324-348. doi: 10.1002/2017JF004529.
- 401 Hartog, A.H. (2017). An introduction to distributed optical fibre sensors. Boca Raton, Florida:  
402 CRC Press/Taylor and Francis.
- 403 Hauck, C., Böttcher, M. & Maurer, H. (2011), A new model for estimating subsurface ice  
404 content based on combined electrical and seismic data sets, *The Cryosphere*, 5(2), 453-468. doi:  
405 10.5194/tc-5-453-2011.
- 406 Hofstede, C., Christoffersen, P., Hubbard, B., Doyle, S.H., Young, T.J., Diez, A., Eisen, O. &  
407 Hubbard, A. (2018), Physical conditions of fast glacier flow: 2. Variable extent of anisotropic ice

- 408 and soft basal sediment from seismic reflection data acquired on Store Glacier, West Greenland,  
 409 *Journal of Geophysical Research: Earth Surface*, *123*, 349-362. doi: 10.1002/2017JF004297.
- 410 Karlsson, N.B., Dahl-Jensen, D., Gogineni, S.P. & Paden, J.D. (2013), Tracing the depth of the  
 411 Holocene ice in North Greenland from radio-echo sounding data, *Annals of Glaciology*, *54*, 44-  
 412 50. doi:10.3189/2013A0G64A057.
- 413 King, E.C., Smith, A.M., Murray, T. & Stuart, G. (2008), Glacier-bed characteristics of midtre  
 414 Lovénbreen, Svalbard, from high-resolution seismic and radar surveying, *Journal of Glaciology*,  
 415 *54(184)*, 145-156. doi: 10.3189/002214308784409099.
- 416 Kulesa, B., Booth, A.D., O’Leary, M., King, E.C., Luckman, A.J., Holland, P.R., Jansen, D.,  
 417 Bevan, S.L., Thompson, S.S. & Hubbard, B. (2019), Seawater softening of suture zones inhibits  
 418 fracture propagation in Antarctic ice shelves, *Nature Communications*, *10*, 5491, 1-12.  
 419 10/1038/s41467-019-13539-x.
- 420 Kuvshinov, B.V. (2015), Interaction of helically wound fibre-optic cables with plane seismic  
 421 waves, *Geophysical Prospecting*, *64(3)*, 671-688. doi: 10.1111/1365-2478.12303.
- 422 Köhler, A., Maupin, V., Nuth, C. & van Pelt, W. (2019), Characterization of seasonal glacial  
 423 seismicity from a single-station on-ice record at Holtedahlfonna, Svalbard, *Annals of Glaciology*,  
 424 *60(79)*, 23-36. doi: 10.1017/aog.2019.15.
- 425 Lira, J.E., Weglein, A.B., Bird, C.W. & Innanen, K.A. (2012), Determination of reflection  
 426 coefficients by comparison of direct and reflected VSP events. *Journal of Seismic Exploration*,  
 427 *21(4)*, 361-376.
- 428 Mateeva, A., Lopez, J., Potters, H., Mestayer, J., Cox, B., Kiyashchenko, D., Wills, P., Grandi,  
 429 S., Hornman, K., Kuvshinov, B., Berlang, W., Yang, Z. & Detomo, R. (2014). Distributed  
 430 acoustic sensing for reservoir monitoring with vertical seismic profiling. *Geophysical*  
 431 *Prospecting*, *62(4)*, 679-692. doi: 10.1111/1365-2478.12116.
- 432 Nanthikesan, S. & Shyam Sunder, S. (1994), Anisotropic elasticity of polycrystalline ice  $I_h$ . *Cold*  
 433 *Regions Science and Technology*, *22*, 149-169. doi: 10.1016/0165-232X(94)90026-4.

- 434 Peters, L.E., Anandakrishnan, S., Holland, C.W., Horgan, H.J., Blankenship, D.D. & Voigt, D.E.  
435 (2008). Seismic detection of a subglacial lake near the South Pole, Antarctica, *Geophysical*  
436 *Research Letters*, *35*, L23501. doi: 10.1029/2008GL035704.
- 437 Peters LE, Anandakrishnan S, Alley RB and Voigt DE (2012). Seismic attenuation in glacier ice:  
438 a proxy for englacial temperature. *Journal of Geophysical Research: Earth Surface*. 117, F02008.  
439 10.1029/2011JF002201.
- 440 Podolskiy, E.A. & Walter, F. (2016), Cryoseismology, *Reviews of Geophysics*, *54*, 7087-758.  
441 doi: 10.1002/2016RG000526.
- 442 Polom, U., Hofstede, C., Diez, A. & Eisen, O. (2014), First glacier-vibro seismic experiment –  
443 Results from cold firn of Colle Gnifetti, *Near Surface Geophysics*, *12(4)*, 493-504. doi:  
444 10.3997/1873-0604.2013059.
- 445 Rignot, E., Box, J.E., Burgess, E., & Hanna, E. (2008), Mass balance of the Greenland ice sheet  
446 from 1958 to 2007, *Geophysical Research Letters*, *35*, L20502. doi: 10.1029/2008GL035417
- 447 Rössli, C., Walter, F., Husen, S., Andrews, L.C., Lüthi, M.P., Catania, G.A. & Kissling, E.  
448 (2014), Sustained seismic tremors and icequakes detected in the ablation zone of the Greenland  
449 ice sheet, *Journal of Glaciology*, *60(221)*, 563–575. doi: 10.3189/2014JoG13J210.
- 450 Smith, E.C., Baird, A.F., Kendall, J.M., Martín, C., White, R.S., Brisbourne, A.M. & Smith,  
451 A.M. (2017), Ice fabric in an Antarctic ice stream interpreted from seismic anisotropy.  
452 *Geophysical Research Letters*, *44*, 3710-3718. doi: 10.1002/2016GL072093.
- 453 Weeks, W. & Assur, A. (1967), The Mechanical Properties of Sea Ice. US Army, Cold Regions  
454 Research and Engineering Laboratory, Monograph 11-C3.